



RESEARCH ARTICLE

Special Feature: Innovation In Practice

UAV-derived greenness and within-crown spatial patterning can detect ash dieback in individual trees

W. R. M. Flynn^{1,2}  | S. W. D. Grieve^{1,3} | A. J. Henshaw¹ | H. J. F. Owen⁴ |
R. J. A. Buggs^{5,6} | C. L. Metheringham^{5,6} | W. J. Plumb^{5,6,7} | J. J. Stocks^{5,6} | E. R. Lines⁵ 

¹School of Geography, Queen Mary University of London, London, UK; ²Department of Plant Sciences, University of Cambridge, Cambridge, UK; ³Digital Environment Research Institute, Queen Mary University of London, London, UK; ⁴Department of Geography, University of Cambridge, Cambridge, UK; ⁵School of Biological and Behavioural Sciences, Queen Mary University of London, London, UK; ⁶Royal Botanic Gardens, Kew, Richmond upon Thames, UK and ⁷Forestry Development Department, Dublin, Republic of Ireland

Correspondence

W. R. M. Flynn

Email: w.r.m.flynn@qmul.ac.uk

Funding information

UK Research and Innovation, Grant/Award Number: MR/T019832/1; The London NERC Doctoral Training Partnership, Grant/Award Number: NE/L002485/1

Handling Editor: Marc Cadotte

Abstract

1. Ash Dieback (ADB) has been present in the UK since 2012 and is expected to kill up to 80% of UK ash trees. Detecting and quantifying the extent of ADB in individual tree crowns (ITCs), which is crucial to understanding resilience and resistance, currently relies on visual assessments which are impractical over large scales or at high frequency. The improved imaging capabilities and declining cost of consumer UAVs, together with new remote sensing methods such as structure from motion photogrammetry (SfM) offers potential to quantify the fine-scale structural and spectral metrics of ITCs that are indicative of ADB, rapidly, and at low-cost.
2. We extract high-resolution 3D RGB point clouds derived from SfM of canopy ash trees taken monthly throughout the growing season at Marden Park, Surrey, UK, a woodland impacted by ADB. We segment ITCs, extract green chromatic coordinate (g_{cc}), and test the relationship with visual assessments of crown health. Next, we quantify spatial patterning of dieback within ITCs by testing the relationship between internal variation of g_{cc} and path length, a measure of the distance from foliage to trunk, for small clusters of foliage.
3. We find g_{cc} correlates with visual assessments of crown health throughout the growing season, but the strongest relationships are in measurements taken after peak greenness, when the effects of ADB on foliage are likely to be most prevalent. We also find a negative relationship between g_{cc} and path length in infected trees, indicating foliage loss is more severe at crown extremities.
4. We demonstrate a new method for identifying ADB at scale using a consumer-grade 3D RGB UAV system and suggest this approach could be adopted for widespread rapid monitoring. We recommend the optimum time of year for data acquisition, which we find to be an important factor for detecting ADB. Although

This is an open access article under the terms of the [Creative Commons Attribution](https://creativecommons.org/licenses/by/4.0/) License, which permits use, distribution and reproduction in any medium, provided the original work is properly cited.

© 2024 The Author(s). *Ecological Solutions and Evidence* published by John Wiley & Sons Ltd on behalf of British Ecological Society.

here applied to ADB, this framework is applicable to a multitude of drivers of crown dieback, presenting a method for identifying spectral-structural relationships which may be characteristic of disturbance type.

KEYWORDS

disease detection and monitoring, RGB, SfM, spatial patterning, UAV

1 | INTRODUCTION

Ash Dieback (ADB) is caused by the invasive fungal pathogen *Hymenoscyphus fraxineus* and has been present in the UK since 2012. It is expected to kill up to 80% of UK ash trees (Coker et al., 2019), impacting the UK economy negatively by billions of pounds through the loss of ecosystem services (Hill et al., 2019). In any epidemic, identifying infection is a crucial first step for monitoring and response (Chan et al., 2021; Liebhold et al., 2017). Currently, the main method for identifying the presence of ADB and the severity of its impact are ground-based surveys of crown cover for large trees, or visual assessments of branch damage for smaller trees (Pliūra et al., 2011; Stocks et al., 2017). These visual assessments are time consuming and ineffective over large scales, leading to insufficient observations for effective monitoring. Large-scale classification of ADB is of particular importance as a degree of genetic resistance has been shown in a small proportion of individuals. This has led to interest in identification of healthy and hence potentially resistant individuals for restoration but a fast and effective method for large-scale phenotyping of intermediate damage is currently lacking (Villari et al., 2018).

Measurement from aerial platforms offers a high-resolution large-scale alternative to ground sampling. New, low-cost remote sensing methods utilising sensors mounted on consumer-grade uncrewed aerial vehicles (UAVs) offer a cheaper alternative to ground-based surveys for monitoring the effects of disease and disturbance (Dandois & Ellis, 2013; Danson et al., 2018; Stone & Mohammed, 2017). UAV structure from motion (SfM)—3D reconstructions of objects created from thousands of overlapping images—provide point-level red-green-blue (RGB) colour information, linking tree and crown structural data with spectral data for the calculation of vegetation indices (Vis; Kerkech et al., 2018; Shendryk et al., 2016). Previous work has shown greenness vegetation indices calculated from RGB data correlate with crown health (e.g. green chromatic coordinate, g_{cc} , and excess greenness, ExG; Reid et al., 2016), indicating an opportunity to measure ADB using low-cost RGB sensors over large spatial and temporal scales.

The lifecycle of causal agent, *H. fraxineus* has a temporal effect on crown dynamics that could impact the effectiveness of crown health monitoring (Stone & Mohammed, 2017). *H. fraxineus* is heterothallic, reproducing sexually once a year within the previous seasons' leaf litter, displaying a seasonal life cycle played out entirely on *F. excelsior* leaves (Gross et al., 2012). In the spring, when new leaves appear, they grow unexposed to *H. fraxineus*, which

has not yet released spores, and appear asymptomatic of the disease. Apothecia are formed during the wet summer months and release ascospores, infecting the new leaf material in the canopy (Timmermann et al., 2011). Ascospores are deposited on the leaf surface and penetrate the leaf cuticle via appressoria leading to lesions on the leaves approximately 2 weeks after infection, and ultimately, severe crown defoliation (Cleary et al., 2013), resulting in changes to the overall crown "greenness" that can be clearly identified visually and with RGB sensors. Detection with RGB sensors may be most effective when leaves have become infected, wilted, and shed, which occurs later in the growing season. Eventually, severely affected trees develop epicormic growth, the rapid appearance of small shoots, on their branches and lower trunk (Gross et al., 2012). Although the effectiveness of surveillance timings has been explored more generally, (e.g. Wardlaw et al., 2008), to date there has been no investigation into the most suitable period within the growing season for ADB detection and monitoring from remote sensing data in the UK.

Although RGB-derived VIs have been shown to be a reliable indicator of stand health, VIs alone cannot identify the causes of damage to the canopy (Reid et al., 2016), necessitating additional interpretation. Numerous attempts have been made to identify forest disturbance types by analysing spectral signatures in airborne and spaceborne hyperspectral imagery (Stahl et al., 2023). Hyperspectral data analysis is indeed a powerful tool, proven to be invaluable for plant phenology and health monitoring (e.g. Gamon et al., 2016; Seyednasrollah et al., 2019; Wang et al., 2023). However, the coarse scale of commonly available satellite data makes individual tree crown identification impossible (Chan et al., 2021), whilst the high cost of acquiring airborne hyperspectral imagery limits monitoring (Dalponte et al., 2012). Recent advances in high-resolution 3D remote sensing provide new measurements of forest structure in detail that far surpass traditional surveying (Lines et al., 2022) and may reveal new insights that draw links between disturbance symptoms and causal agents (Stone & Mohammed, 2017). The cause of dieback could influence the spatial patterning of crown damage in individual trees. For example, Stephenson et al. (2018) found that drought-induced dieback in giant sequoias occurred in shoots proximal to the main stem, in a process caused by drought-triggered senescence preferentially retaining younger shoots. The structural response to ADB may be functionally different, as symptoms initially occur in the younger crown regions (Bengtsson et al., 2014; Skovsgaard et al., 2010), which may lead to a characteristic spatial patterning in crown responses identifiable from aerial monitoring.

Initial responses to *H. fraxineus* at the leaf-level include development of necrotic lesions on petioles and young shoots, rachises and leaflet veins, followed by leaf wilting and shedding (Krätzler & Kirisits, 2012), leading to crown dieback, which is accompanied by epicormic growth.

Multiple studies have combined spectral and structural data in an attempt to improve disease classification accuracy by combining airborne multi- or hyper-spectral data with LiDAR data (e.g. Kantola et al., 2010; Shendryk et al., 2016). However, the high cost of collecting airborne data combined with the computational difficulties of co-registering multi-sensor measurements limit their widespread utility (Dalponte et al., 2012). Using RGB imagery with SfM from UAVs, spectral and structural data can be collected concurrently at ultra-high resolution and relatively low cost (Cessna et al., 2021; Stone & Mohammed, 2017), and the recent rapid increase in accessibility of UAV technology now make them a practical tool for widespread use. Although multispectral LiDAR has been available for some time (Hopkinson et al., 2016), it has not yet been widely adopted by the community, due to the complexity and cost. The additional RGB data in SfM, unavailable from conventional LiDAR data alone, has been shown to improve species classification, phenological stage detection, structure, and forest health monitoring in UAV data (Alonzo et al., 2020), although whether accuracy is comparable to hyperspectral imagery and LiDAR fusion is unclear (Alonzo et al., 2020; Cessna et al., 2021). Nevertheless, SfM models generated from high forward overlap (>90%) imagery have been shown to produce photogrammetric models capable of penetrating to the forest floor (Dandois et al., 2015; Frey et al., 2018), and have the potential to map fine-scale structural attributes of individual tree crowns (ITCs) at higher spatial resolution than airborne systems. For example, using high-resolution structural and spectral data from UAV-derived SfM, Cessna et al. (2021) were able to detect crown defoliation by assessing the vertical gradient of greenness through the canopy.

In this study, we use UAV-derived RGB SfM data to calculate multi-temporal whole-crown and 3D cluster-based greenness in 120 canopy ash trees at Marden Park, Surrey: A Woodland Trust-owned mixed broadleaved woodland impacted by ADB. We compare expert visual ground assessments of crown health with our UAV-derived metrics and answer the following questions:

1. Can we accurately measure key 2D (tree height, crown area and maximum crown diameter) and 3D (convex crown volume) structural metrics using low-cost consumer uncrewed aerial vehicle imaging and structure from motion photogrammetry.
2. Can we accurately detect ash dieback in individual tree crowns using low-cost consumer uncrewed aerial vehicle imaging and SfM photogrammetry?
3. At what time in the growing season is ash dieback detection from uncrewed aerial vehicle data most effective?
4. Does ash dieback produce specific spatial patterns of greenness within individual tree crowns identifiable from uncrewed aerial vehicle, red-green-blue, structure from motion data?

2 | MATERIALS AND METHODS

2.1 | Study site and expert assessment

Marden Park is a 67-ha ancient broadleaved woodland, located on the North Downs in East Surrey, UK. The site is an Area of Outstanding Natural Beauty (AONB) and a Site of Special Scientific Interest (SSSI), situated on a chalk plateau ~244 m a.s.l. We established a plot of size 0.6 ha containing 120 canopy ash (*F. excelsior*) trees, of which 47 were visually assessed for dieback severity using a scoring of 0%–100% remaining live crown on 18–19 August 2021 (Metheringham et al., 2022). The plot has a crown area index (total crown area divided by ground area) of 0.3, as calculated from UAV SfM data collected in May 2021 (detailed description of canopy and understorey density provided in Supporting Information, Section S13). The area is secondary broadleaf woodland, approximately 60 years old and is approximately 80% ash (*Fraxinus excelsior*) dominant with beech (*Fagus sylvatica*) the secondary dominant species. Site access and permission to work was granted by the Woodland Trust.

2.2 | UAV data collection and pre-processing

2.2.1 | SfM collection and pre-processing

We collected images in September–October 2020 and each month May–August 2021 using a DJI Mavic Mini UAV. A complete growing season was captured over two successive calendar years (sampling was restricted by regulations related to control of Covid-19). The UAV has a take-off weight of 249 g, maximum flight time of 30 mins, maximum wind resistance of 8 ms^{-1} and it is equipped with a the standard DJI Mini 12 MP RGB sensor with 83° field of view and aperture f/2.8. Flights were carried out at two altitudes (50 m (ground sample distance (GSD): 1.78 cm/2.17 cm nadir/oblique), and 70 m (GSD: 2.49 cm/ 3.04 cm nadir/oblique) above take-off location, which was consistent for all flights) and two camera angles (nadir flights at -90° referenced to the horizon, and oblique flights at -55° degrees referenced to the horizon). Combining flight altitudes provides the higher ground sampling resolution of low altitude with the wider field of view of high altitude (Roşca et al., 2018), while combining nadir with high oblique angle imagery (20–35° off nadir) increases point cloud resolution and accuracy (Nesbit & Hugenholtz, 2019). We captured images with a front overlap of 95% and side overlap of 80% over an area 3.2 ha centred on the 0.6 ha study plot in order to avoid edge effects distorting reconstruction (Mohan et al., 2021). Consumer sensors have multiple parameters for image acquisition including focal length, shutter speed, and white balance; the effects of these parameters on image acquisition are interdependent and dependent on individual scene lighting conditions and camera angle, and, in the case of focal length, altitude and distance from canopy (Frey et al., 2018). To minimise potential differences caused by maintaining parameters in images acquired across multiple flight

altitudes, camera viewing angles, sky conditions and seasonality, we set these camera parameters to 'auto' (Dandois et al., 2017). Flight paths were programmed using the automatic flight generation software *dronelink* (version 3.3.1) and were consistent for all flights. We placed nine checkerboard ground control points (GCPs) in canopy gaps around the perimeter and in the centre of the plot, located to capture topographic variation in the X, Y, Z planes and designed to be clearly visible from the UAV imagery, for SfM point cloud reconstruction and co-registration of SfM and TLS point clouds. We recorded the precise location of their centres using a Leica Total Station in an arbitrary local cartesian coordinate system (m) and marked the location of each target with a wooden stake so the same location could be used in each data acquisition campaign. We removed UAV-GPS location stamps from individual images, using the Total Station measurement GCP locations for increased accuracy. We constructed SfM point clouds using *Agisoft Metashape* (version 1.7.4), manually removing images with visible blur before aligning with 'high' accuracy, disabling generic preselection and generating a dense cloud with 'high' quality (Roşca et al., 2018; Tinkham & Swayze, 2021). We validated the accuracy of SfM point clouds using co-registered high-resolution terrestrial laser scanning (TLS) data (see Section 2.3.2).

Point cloud filtering is an essential step to remove erroneous points in SfM point clouds caused by image blur and poor camera alignment, or vegetation movement caused by wind (Tinkham & Swayze, 2021). We used a statistical outlier removal (SOR) filter and Euclidean cluster filter to remove sparse outliers and isolated clusters from raw SfM point clouds. An SOR filter removes points with a distance greater than a user-defined number of standard deviations ($SD=1$) from the neighbourhood average ($k=100$), removing sparse outliers. To remove small, isolated clusters missed by the SOR algorithm, we applied a Euclidean clustering algorithm with a defined minimum distance between points of 0.5 m, and removed any that contained less than 1000 points, ensuring no removal from within individual tree crowns. Combining an SOR filter and Euclidean cluster filter in this way, both noisy isolated points along with larger groups of noise that can emerge from SfM processing are removed. We applied these filters using the Point Cloud Library (PCL; Rusu & Cousins, 2011). Finally, we downsampled point clouds to a point-to-point minimum distance (resolution) of 0.05 m to aid computational time, while retaining fine-scale structural features of the point cloud (Owen et al., 2021).

2.2.2 | TLS collection and pre-processing

To segment individual trees from our SfM data, we used a co-registered TLS dataset of semi-automatically delineated trees to provide the most accurate results. Many current segmentation algorithms rely on cylinder fitting, requiring accurate reconstruction of the lower stem (e.g. Burt et al., 2019; Krisanski et al., 2021), and are therefore less effective with above-canopy captured UAV data due to occlusion from the upper canopy (see Section 2.2.3). We

also used the same TLS dataset in an intermediate step to validate 2D and 3D crown metrics extracted from individual tree point clouds. We scanned the 0.6 ha plot at Marden Park in May 2021 using a Riegl VZ400i TLS in May 2021. Scan locations were placed on a grid, 10 m apart, (Owen et al., 2021; Wilkes et al., 2017); however, some scan locations were spaced further due to forest understorey vegetation density, with 58 scan locations in total. For each location, scans were collected in the upright and horizontal positions capturing the full field of view of the scanner, resulting in 116 scans. We filtered the co-registered scans using an SOR and Euclidean filter as described in Section 2.2.1, using PCL and downsampled to 0.05 m, matching the resolution of SfM point clouds. We semi-automatically segmented individual tree crowns, including stems within a 10 m buffer around the plot, using the Forest Structural Complexity Tool (FSCT; Krisanski et al., 2021), and followed this by manual refinement of point clouds. Finally, we labelled trees for which we had visual assessments ($n=47$; total delineated trees = 120) using a co-registered stem map generated using a Leica Total Station and co-registered the TLS and SfM point clouds using GCP locations captured by both sensors using a 3D rotation matrix in CloudCompare (cloudcompare.org).

2.2.3 | Individual tree segmentation in SfM point clouds

We followed a point neighbourhood approach to segment individual tree point clouds from the SfM data using delineated TLS point clouds (see Section 2.2.2; Figure 1). This enables an effective buffer to be created around the TLS data to account for variation due to movement or growth. A K-dimensional tree was built around the SfM plot point cloud and queried for nearest neighbours based on the TLS point cloud (Figure 1a) within a user-defined maximum distance (0.25 m). Nearest neighbour points were then matched to the raw SfM cloud (Figure 1b,c) and individual SfM trees were segmented (Figure 1d). SfM segmentation was carried out using the *Open3D* Library in Python (Zhou et al., 2018).

2.3 | Extracting metrics

2.3.1 | Automated crown base detection

To determine crown greenness, we needed to separate crown and stem points to avoid erroneously including the trunk. For each individual SfM tree point cloud, we segmented the tree crown by vertically slicing the tree (*slice height*=0.05 m) and measuring the width of each slice. Iterating downwards from the top of the tree, we defined the base of the crown to be at the height at which the moving average of previous slices decreases by a factor of at least 0.5 and segmented the crown above this line (Figure 2). We performed this automatic crown segmentation separately for each tree in each survey.

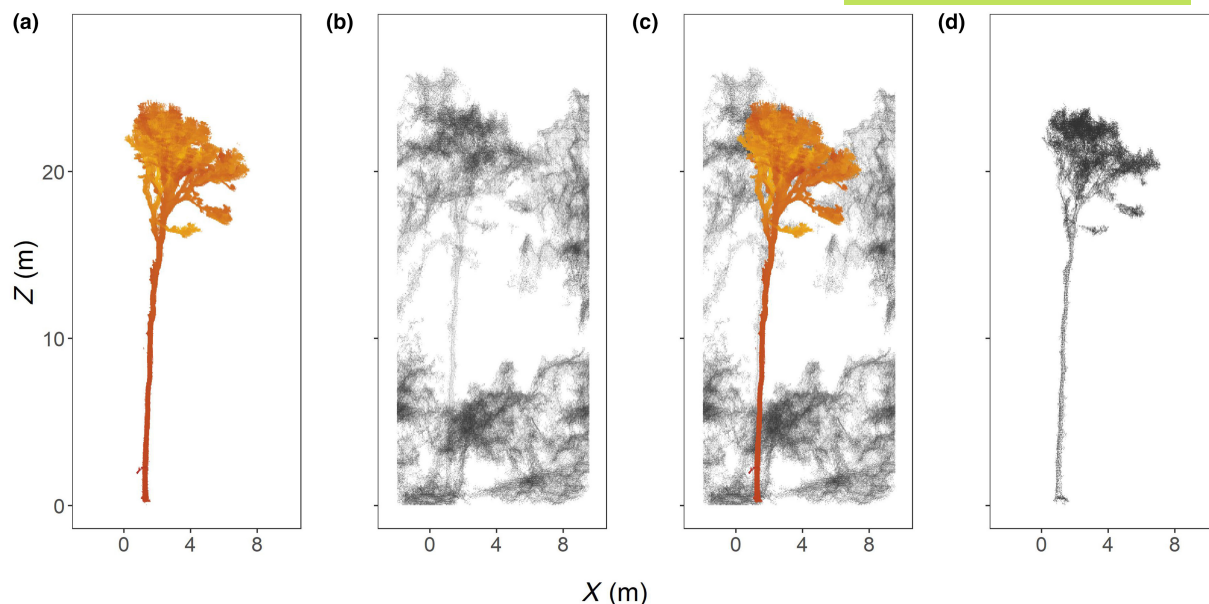


FIGURE 1 Example schematic showing the individual SfM tree segmentation process. (a) A semi-automatically segmented TLS tree ($\sim 14,000$ pts/m²) segmented using the Forest Structural Complexity Tool (FSCT; Krisanski et al., 2021) and manual cleaning; (b) a section of raw SfM point cloud (grey points); (c) a section of raw SfM point cloud (grey points) with the segmented TLS tree (coloured points) overlaid. and (d) a segmented SfM tree point cloud (~ 1000 pts/m²) extracted within a maximum point distance (0.25 m) from a KD-tree built from the segmented TLS tree point cloud using the Open3D library in Python (Zhou et al., 2018). TLS tree was scanned on 2020-03-15 and SfM tree was scanned on 2021-07-21, demonstrating the ability of this method to capture the same tree throughout the growing season.

2.3.2 | Validating SfM-derived ITC point clouds

To quantify crown greenness and spatial patterning of greenness in individual tree crowns measured by UAV-derived SfM, we first validated that our SfM-derived ITC point clouds were accurate by comparing widely used 2D (tree height, crown area and maximum crown diameter) and 3D (convex crown volume) structural metrics with those from the TLS-derived point clouds. We calculated tree height in TLS data as the maximum minus the minimum point Z values, and in SfM data as the maximum point Z value minus an Environment Agency 2018 LiDAR-derived DTM, available at <https://environment.data.gov.uk/> (last accessed on 15 August 2023). We used a 0.05 m resolution digital terrain model (DTM) to provide accurate ground height measurements increase accuracy of estimated tree height in the latter instance, as ground points are limited in UAV-derived data due to occlusion from the top of canopy. In both instances, we calculated crown area and maximum crown diameter using the R package *conconvex* (Gombin et al., 2020) and convex crown volume using the R package *geometry* (Habel et al., 2023).

2.3.3 | Crown greenness and spatial patterning

We used green chromatic coordinate (g_{cc})—the normalised green channel values of individual tree crown points— $g_{\text{mean}} / (r_{\text{mean}} + g_{\text{mean}} + b_{\text{mean}})$. g_{cc} is a commonly used metric for UAV timeseries and phenology analysis (Berra et al., 2016; Larrinaga & Brotons, 2019; Park et al., 2019), and

has been shown to be more robust than other RGB VIs, such as excess greenness (ExG), where measurements have been taken under a range of lighting environments (Sonnentag et al., 2012), as is the case in this study.

To quantify spatial patterns of dieback in individual tree crowns in order to determine if they are indicative of ADB, we calculated the path length of each point in our SfM ITCs using the open-source Python module *TLSeparation* (Vicari et al., 2019). The path length is the distance of a point from the ground along the structure of the tree and is a measure of position within the trees' transport system. In trees under stress, we would expect points at the extremities, for example with longer path lengths, to experience dieback from embolism first. To calculate path length, the individual tree point cloud (crown and stem) is first represented as a network graph where points are nodes with connecting edges. Using the network graph, a shortest path analysis computes the distance from each node, along each edge, to the lowest point in the point cloud (Vicari et al., 2019), assigning a shortest path length to each point in the point cloud. Finally, to reduce noise we clustered groups of points using a density-based spatial clustering of applications with noise (DBSCAN) algorithm, which is effective at grouping 3D data (Giri et al., 2021). For each cluster (*mean size* = 8 points), we then calculated cluster g_{cc} as mean point g_{cc} , and path length to centre of the cluster as the median within cluster point-level path length. Point density varied spatially, but with an approximate average of 1000 pts/m² making a cluster approximately 4 × 4 cm.

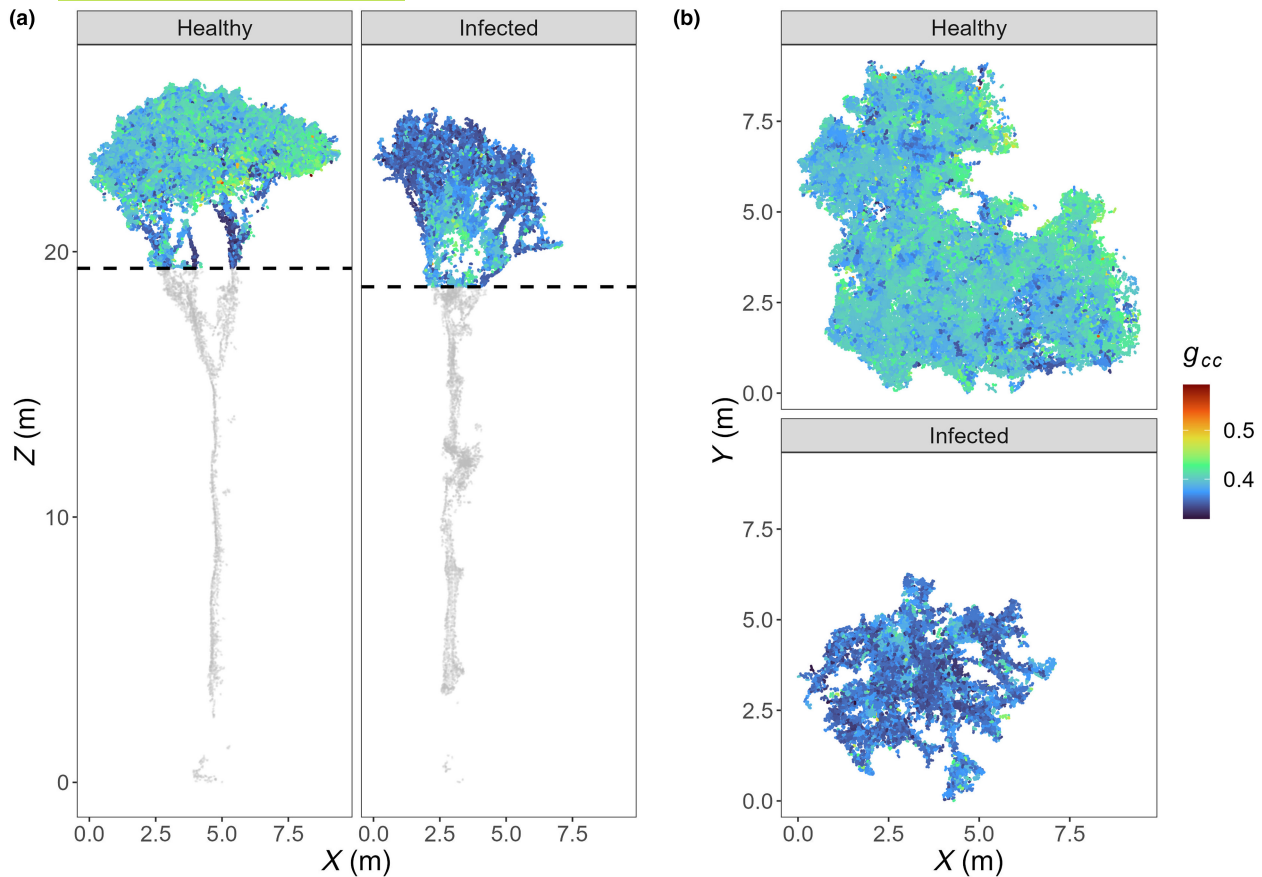


FIGURE 2 Multiple viewpoints of a representative healthy and infected segmented SfM tree point cloud showing mean cluster g_{cc} . Viewpoints: (a) anterior view showing x and z axes; (b) top-down transverse view showing x and y axes. Colour gradient shows mean green chromatic coordinate (g_{cc}) of clustered crown points where blue is low and red is high g_{cc} . Stem points not used in analysis are denoted in grey. Dashed line shows automatically detected crown base. The base of the crowns was detected by slicing the point cloud into vertical slices of height 0.05 m and calculating the moving average of slice width. The base of the crown is detected when the moving average decreases by a factor of at least 0.5. Crown points were clustered using a density-based clustering algorithm implemented using the Python module DBSCAN (Pedregosa et al., 2011).

2.4 | Statistical analyses of whole-tree and within crown g_{cc}

We tested the relationship between individual tree crown g_{cc} values collected in each month of the survey (September–October 2020 and May–August 2021) with visual assessments of crown health, surveyed during 18–19 August 2021, using linear models in the open-source statistical software R (R Core Team, 2023):

$$gcc_{tree} = a \times PLC + b \quad (1)$$

here gcc_{tree} is individual tree crown g_{cc} , PLC is per cent live crown estimated from visual assessments and a and b are parameters to be fit. Visual assessments of crown health comprised expert estimation of per cent live crown within the projected crown area (Metheringham et al., 2022).

To understand the spatial patterns of dieback in infected tree crowns, we categorised trees into two groups based on a threshold generated from the subset of trees that were visually assessed. From this group, we took the minimum g_{cc} value of trees with >70%

live crown and categorised all trees with gcc_{tree} values above this as “healthy” ($n=35$), with the remaining trees classified as “infected” ($n=85$). We based this threshold on a visual inspection of the distribution of greenness values across per cent live crown (Figure S11). Fitting models separately to these ‘infected’ and ‘healthy’ groups, we tested the relationship between cluster g_{cc} and path length by including an intercept only random individual tree effect to account for variation in g_{cc} between individuals:

$$gcc_{i,h,j} = a_h + b_h P_i + treeID_j \quad (2)$$

here gcc_i is the mean cluster g_{cc} of cluster i in individual j of infection category h , P is the median path length of cluster i , $treeID$ is a random effect to account for g_{cc} variation between individuals, and a and b are the parameters to be fit.

For Equation 1, we calculated the coefficient of determination (R^2) to determine the best relationship between UAV-derived g_{cc} and visual assessments of crown health. For Equation 2, we compared slopes of the relationships between cluster g_{cc} and path length.

3 | RESULTS

3.1 | SfM is able to capture tree shape validated by TLS

Of the four structural metrics compared, we found very high correlation between TLS and SfM for both the 2D (tree height: $R^2=0.98$, $p<0.001$; crown area: $R^2=0.99$, $p<0.001$; max crown diameter: $R^2=0.98$, $p<0.001$, Figure 3) and 3D (crown volume: $R^2=0.96$, $p<0.001$, Figure 3) metrics, indicating that SfM-derived point clouds are suitable to measure the structural properties of ITCs. SfM underestimated crown volume (Figure 3d) compared to TLS, which is

likely due to insufficient penetration through the crown from the airborne sensor.

3.2 | g_{cc} performs well as a method to identify severity of ADB impact

We found a statistically significant correlation between measured ITC g_{cc} and visual assessment of crown health for four of the six surveys (2021-06-11: $R^2=0.29$, $p<0.001$; 2021-07-21: $R^2=0.49$, $p<0.001$; 2021-08-17: $R^2=0.49$, $p<0.001$; 2020-09-10 $R^2=0.45$, $p<0.001$; Figure 4). We found no correlation between ITC g_{cc} values and visual assessments at

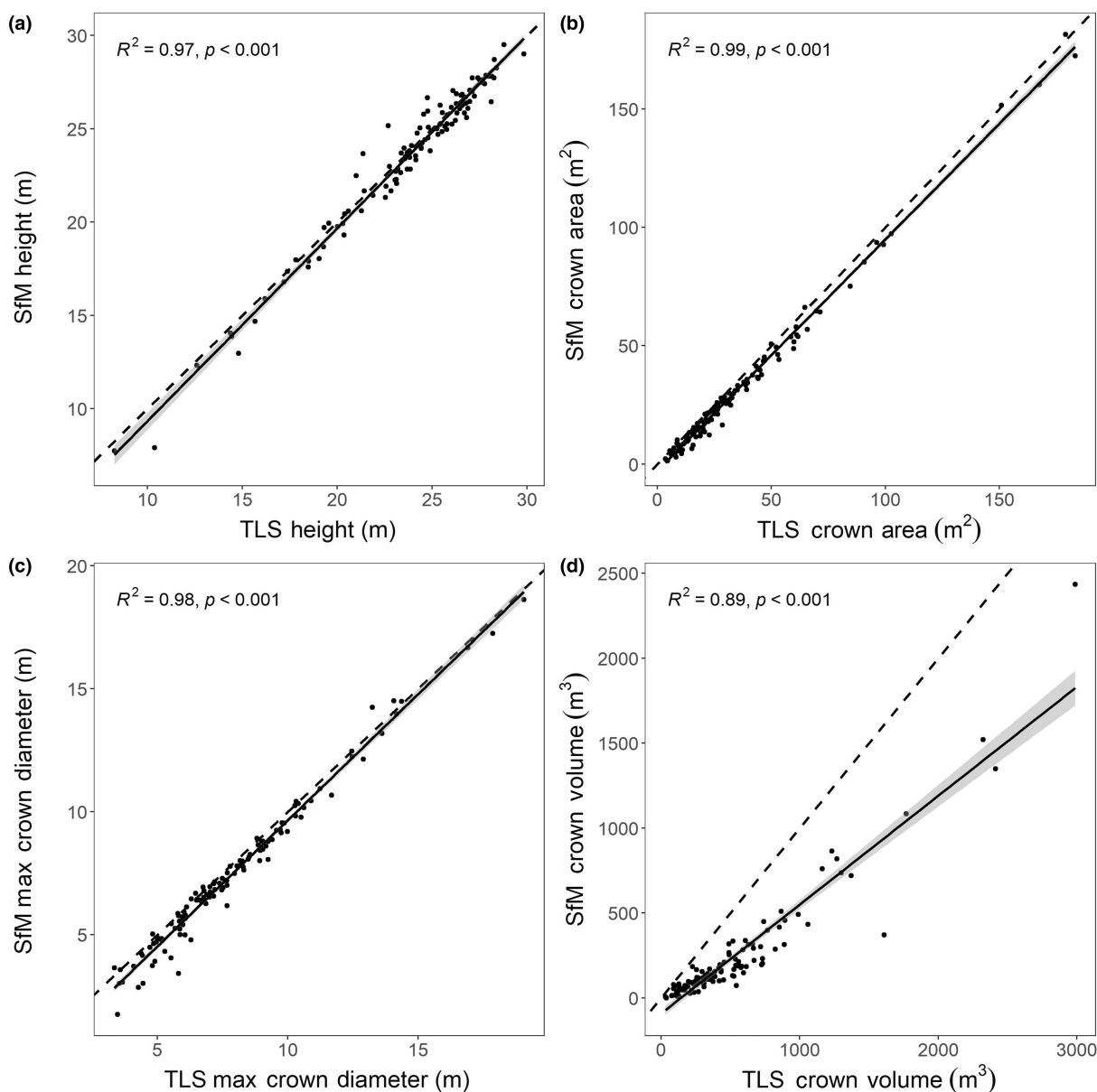


FIGURE 3 Comparison of (a) TLS and SfM Height measurements (b) TLS and SfM crown projected area measurements (c) TLS and SfM measured maximum crown diameter and (d) TLS and SfM measured crown volume. TLS and SfM measurements taken in May 2021. 1:1 line is the dashed line. TLS tree height was calculated as $Z_{\max} - Z_{\min}$ and SfM height was calculated as $Z_{\max} - \text{EA LiDAR DTM}$. Area/ diameter and volume measurements were calculated using the R packages *concaveman* and *geometry*, respectively.

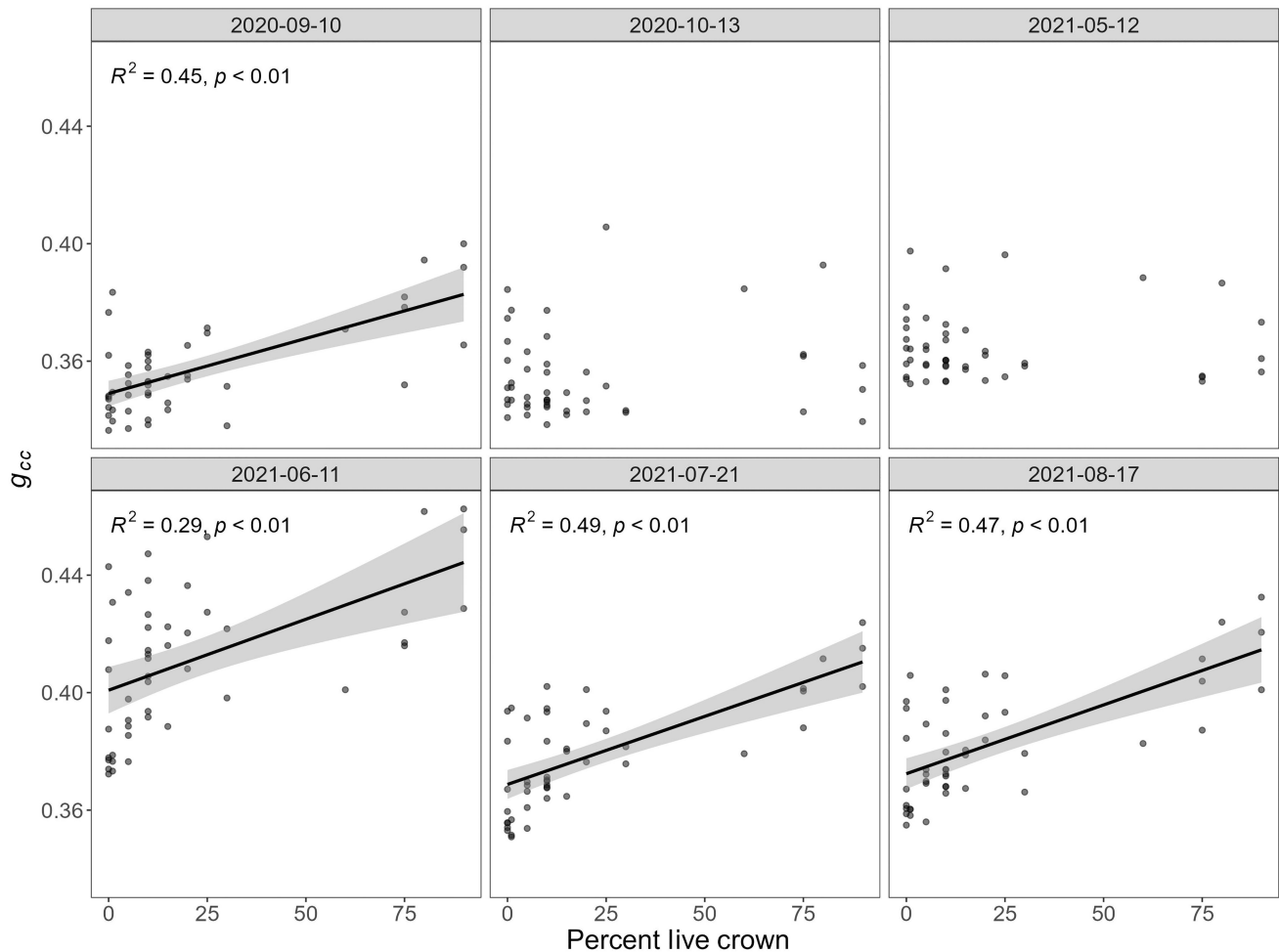


FIGURE 4 The relationship between visual assessment of crown health, defined as per cent live crown and green chromatic coordinate (g_{cc}) throughout the growing season. Visual assessments of crown health were carried out 18–19 August 2021. Solid black lines show statistically significant correlations and grey envelopes show 95% confidence intervals. A representative growing season was captured across both 2020 and 2021 seasons due to covid restrictions.

the beginning (2021-05-12: $p > 0.05$) and end (2020-10-13: $p > 0.05$) of the growing season, which may be due to lower overall foliage levels. The positive correlation between g_{cc} and visual assessments throughout the leaf on season demonstrates that g_{cc} is a consistent indicator of tree health. g_{cc} peaked in June (2021-06-21; [Figure S12](#)), however stronger correlations occurred in measurements taken after peak greenness, suggesting g_{cc} measured later in the growing season may be a better indicator of crown health for trees infected with ADB.

To account for high correlations that may occur from g_{cc} estimates and visual assessments of per cent live crown remaining being acquired at similar dates, we tested the relationship between the same g_{cc} values and visual assessments carried out in 2019 and 2020. We present these results in [Figure S13](#) and found similar patterns to comparisons with 2021 per cent live crown.

3.3 | g_{cc} declines towards the edges of crowns of trees affected by ADB, but increases in healthy trees

As the strongest correlations between g_{cc} and visual assessments of crown health were found in ITCs measured in 2021-07-21, we

used these data to quantify spatial patterns of dieback and found opposite trends in healthy and infected trees. We found a statistically significant positive relationship between path length and g_{cc} in the 35 trees classified as healthy ($a = 0.0002$; 95% CI = 0.00016, 0.00024; $p < 0.001$; [Figure 5](#)) meaning that in healthy trees the outer regions of the crown are greener than in the centre. In infected trees we found the opposite pattern; we found a statistically significant and strong negative relationship between g_{cc} and path length in the 85 trees classified as infected ($a = -0.001$; 95% CI = -0.00096, -0.00104; $p < 0.001$), suggesting that ADB initially infects the extremities of the crown.

4 | DISCUSSION

4.1 | A low-cost method for ADB detection and monitoring with RGB information

Our results, testing the relationship between ITC g_{cc} and visual assessments of crown health, show that UAV-collected RGB data can both detect ADB and assess its severity, providing a significantly

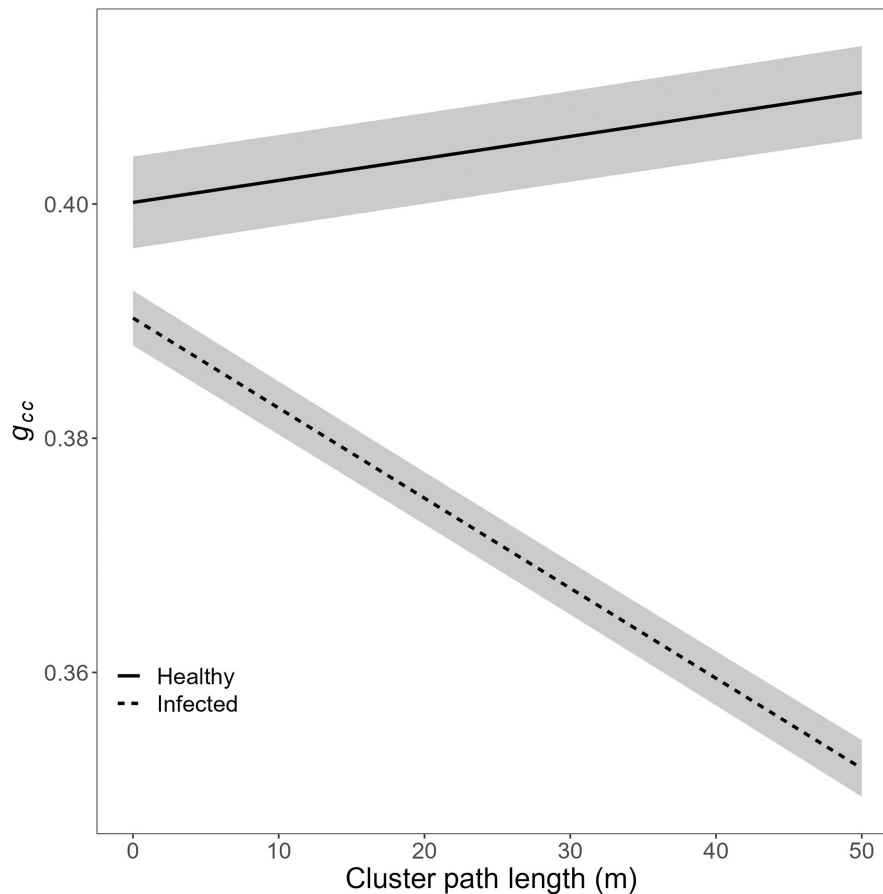


FIGURE 5 Linear mixed models showing the relationship between cluster path length and cluster g_{cc} in 35 healthy (solid line) and 85 infected (dashed line) trees. Trees were classified as healthy or infected using a g_{cc} threshold derived from visual assessments of crown health. ITC points were clustered using the Python module DBSCAN (Giri et al., 2021). Ribbons represent 95% confidence intervals.

lower-cost method for disease detection and monitoring than airborne hyperspectral sensing (e.g. Chan et al., 2021), and supporting previous findings that information on plant physiological stress, chlorophyll content and leaf area index (LAI) alters the magnitude of g_{cc} (Reid et al., 2016; Sankaran et al., 2010; Yang et al., 2014). Such broad spectral band metrics have been shown to be powerful ecological tools, and are better suited for near-sensing applications, as short wavelengths are impacted by atmospheric scattering (Nijland et al., 2014). While hyperspectral data certainly contain more information, our data show that there are large gains to be made at low-cost with broad spectral bands. Indeed, previous work has found only small improvements of narrow band over broad-band VIs (Elvidge & Chen, 1995; Gitelson et al., 1996; Richardson et al., 2018; Vincini & Frazzi, 2011), further strengthening the case for the use of off-the-shelf and accessible consumer RGB-equipped UAVs for disease detection and monitoring. Low-cost RGB information has been impactful in other ecological applications; for instance, the Phenocam network uploads publicly available half-hourly images of sites covering a wide range of plant functional types, environments, and climates (Seyednasrollah et al., 2019), and has revolutionised understanding of global deciduous phenology with accessible and cheap sensors, considerations that are particularly important in regions

with limited access to highly expensive technical instrumentation and computing resources (Manfreda et al., 2018; Richardson, 2019; Sethi et al., 2023).

Although we found good correlation between g_{cc} and visual assessments of crown health, there was unexplained variation remaining in the model. g_{cc} has previously been shown to have high correlation to visual assessments, as spectral bands measured in the visible wavelengths capture information that is interpretable by the human eye (Soudani et al., 2021). However, the different view point of above vs below canopy sampling may introduce additional error, as perspective may alter the damage visible to the sensor (Ho et al., 2022).

Although we relied on high-resolution TLS data to segment trees in UAV-derived SfM data, recent progress in individual tree segmentation is likely to see the development of a full end-to-end pipeline with exclusive use of low-cost UAV data. For example, the Forest Structural Complexity Tool, used here to segment TLS trees, could work more efficiently with UAV data with additional training data (Krisanski et al., 2021). The recently released Segment Anything model (SAM; Kirillov et al., 2023) and *Detectree2* (Ball et al., 2023), as well as multiple neural network applications based on the *PointNet* architecture (e.g. Wielgosz et al., 2023; Yu et al., 2022) show promise to accurately segment trees in 2D and 3D

UAV-derived data. These advances in segmentation algorithms, combined with increased affordability of lightweight consumer UAVs hold the potential to revolutionise ecological applications of low-cost 3D spectral data. Similarly, we used a total station to survey the precise location of GCPs. With the price-point of real-time kinetic positioning-enabled consumer UAVs rapidly decreasing, along with global navigation satellite systems such as the emlid reach series (e.g. Krofcheck et al., 2019) and mavic 3 enterprise series (e.g. Barazzetti et al., 2023) becoming more accessible, the need for GCPs may become redundant (Tomaščík et al., 2019), opening the opportunity for more rapid data collection with fewer specialised equipment costs. However, in dense forest canopies, UAV-derived SfM data will suffer from lower penetration through the canopy due to a larger effective pixel size, meaning LiDAR data is likely to produce more accurate segmentation.

4.2 | ADB detection from UAV data is most effective after peak greenness

A key determinant in the efficiency and accuracy of forest health monitoring is timing; a successful survey should be carried out when the symptoms of the pathogen are most prevalent (Wardlaw et al., 2008). We found the strongest correlation between g_{cc} and visual assessments of crown health in data collected immediately after peak greenness, in July, with the next strongest correlations for the August and September surveys. Here, we demonstrate that ideal survey timing broadly follows the patterns we would expect from prior knowledge of ADB dynamics, where ascomata of *H. fraxineus* typically form in July–August (Timmermann et al., 2011) and lesions appear on leaves approximately 2 weeks after inoculation (Gross et al., 2012). Although it has previously been found that ADB surveys are best carried out in the summer leaf-on months (Stocks et al., 2017), we present analysis defining the best month for detection. While precise timings are likely to be impacted year-to-year by environmental and climatic factors such as temperature, soil moisture and rainfall, we show a clear pattern of higher correlations after peak greenness, corroborated by the previous 2 years' data.

A key benefit of UAV-derived monitoring is ease of data acquisition; collecting data cheaply and quickly means repeat surveys can be carried out with high temporal resolution (van Iersel et al., 2018) requiring minimal operator training. This means that repeat measurements of g_{cc} , shown here to correlate to visual assessments of crown health, could be taken routinely, allowing the rate of ADB severity progression and shifts in phenological patterns to be monitored, providing key metrics for managing impacts of disease (Stone & Mohammed, 2017).

4.3 | Spatial patterns of dieback can help to identify causes of disturbance

In this study, we provide evidence that characterising spatial patterns of greenness within ITCs may help identify dieback drivers. Our results

show an opposite relationship between g_{cc} and path length in infected versus healthy trees. This finding supports evidence that UAV-derived SfM data can refine detection and map fine-scale location-specific foliage changes (Cessna et al., 2021) previously only possible with multi- and hyper-spectral–LiDAR fusion (Cho et al., 2012; Dalponte et al., 2012; Kantola et al., 2010; Shendryk et al., 2016). Studies using high-resolution 3D data to quantify internal patterns of dieback have so far been limited, however there is a growing body of evidence for driver-characteristic spatial patterning. For example, trees influenced by drought events have been shown to display early senescence, which can retain young, distal buds and shoots (Jump et al., 2017; Munné-Bosch & Alegre, 2004), and simple visual assessments of tree crown imagery have shown dieback proximal to the lower stem in trees impacted by drought (Stephenson et al., 2018). Similarly, defoliation caused by spruce bark beetle appears to occur in the older foliage, situated in the upper, inner canopy, and has been shown to be measurable by UAV-derived SfM data (Cessna et al., 2021). Here, we quantify the spatial patterns of defoliation associated with ADB, while improving classification by filtering signal from below canopy vegetation, which is known to influence quantification of ADB severity (Chan et al., 2021). However, more work using 3D measurements of internal ITC dieback is needed to understand fine-scale spatial variation in response to multiple specific drivers of disturbance. Although here applied to ADB, this framework is applicable to a multitude of drivers of dieback, presenting an ideal method for identifying spectral-structural relationships which may be characteristic of disturbance type.

We found a stronger relationship between cluster path length and g_{cc} (defined by 95% CIs) in infected trees than healthy ones; however, this may be caused by the smaller sample size ($n=35$ for healthy trees). Once ADB is present in a geographical region, it spreads quickly and therefore many of the healthy trees are situated close to infected ones and may be inoculated at an early stage of infection (Stocks et al., 2017). On the other hand, trees classified as healthy in close proximity to trees classified as infected, and *not* showing the spatial patterns of dieback, could indicate genetic resistance. More work is required to draw links between genetic breeding values and measurements of dieback severity to understand if genetic resistance can be predicted via remotely sensed data.

5 | CONCLUSIONS

We show ITC g_{cc} is a good indicator of crown health in trees infected with ADB by comparing with visual assessments of per cent live crown. We also used repeat measurements to identify that the best time of year for ADB surveillance is during the growing season, after peak greenness. Finally, we map the fine-scale spatial patterns of internal crown greenness to help identify ADB in remotely sensed data. Our results demonstrate a new low-cost method to detecting ADB and mapping severity, previously only possible with expensive hyperspectral imagery, demonstrating the importance of fine-scale structural data for quantifying forest dynamics and ecological monitoring. This builds

on previous work, for example classifying tree species from structural information alone (Allen et al., 2022; Terryn et al., 2020), highlighting a movement towards the co-measurement of structural and functional traits with high-resolution remote sensing (Lines et al., 2022).

We demonstrate the power of structural measurements to detect fine-scale ecological signal by showing that the spatial arrangement of greenness in ITCs can be indicative of causal agents of dieback. We therefore propose that this work demonstrates the opportunity to map dieback in ITCs from various causes, providing a new framework for classifying drivers of disturbance through an intercomparison of remotely sensed data.

AUTHOR CONTRIBUTIONS

William Rupert Moore Flynn, Stuart William David Grieve, Alex James Henshaw and Emily Rebecca Lines conceived the ideas and designed methodology; William Rupert Moore Flynn and Emily Rebecca Lines collected the UAV and TLS data, with help from numerous field assistants; Richard Buggs, Carey Louise Metheringham, William Plumb and Jonathan Stocks established the study site and made the visual assessments of crown health. William Rupert Moore Flynn analysed the data with guidance from all authors; WRMF led the writing of the manuscript. All authors contributed critically to the drafts and gave final approval for publication.

ACKNOWLEDGEMENTS

William Rupert Moore Flynn was funded through a London NERC Doctoral Training Partnership. Emily Rebecca Lines, Harry Jon Foord Owen and Stuart William David Grieve were funded through the UKRI Future Leaders Fellowship awarded to Emily Rebecca Lines (MR/T019832/1). The authors would like to thank the Woodland Trust for providing access to the study site and field assistants Matt Allen, Jordan Bull, Jessica Hothersall, and Jason Lynch for their support collecting UAV data.

CONFLICT OF INTEREST STATEMENT

The contact author has declared that none of the authors has any competing interests.

PEER REVIEW

The peer review history for this article is available at <https://www.webofscience.com/api/gateway/wos/peer-review/10.1002/2688-8319.12343>.

DATA AVAILABILITY STATEMENT

Individual cluster g_{cc} and pathlength values for each tree used in this study can be found on Zenodo: <https://doi.org/10.5281/zenodo.11191314> Flynn et al. (2024).

ORCID

W. R. M. Flynn  <https://orcid.org/0000-0002-7426-4186>

E. R. Lines  <https://orcid.org/0000-0002-5357-8741>

REFERENCES

Allen, M. J., Grieve, S. W. D., Owen, H. J. F., & Lines, E. R. (2022). Tree species classification from complex laser scanning data in

Mediterranean forests using deep learning. *Methods in Ecology and Evolution*, 14, 1657–1667. <https://doi.org/10.1111/2041-210X.13981>

- Alonzo, M., Dial, R. J., Schulz, B. K., Andersen, H.-E., Lewis-Clark, E., Cook, B. D., & Morton, D. C. (2020). Mapping tall shrub biomass in Alaska at landscape scale using structure-from-motion photogrammetry and lidar. *Remote Sensing of Environment*, 245, 111841. <https://doi.org/10.1016/j.rse.2020.111841>
- Ball, J. G. C., Hickman, S. H. M., Jackson, T. D., Koay, X. J., Hirst, J., Jay, W., Archer, M., Aubry-Kientz, M., Vincent, G., & Coomes, D. A. (2023). Accurate delineation of individual tree crowns in tropical forests from aerial RGB imagery using Mask R-CNN. *Remote Sensing in Ecology and Conservation*, 9, 641–655. <https://doi.org/10.1002/rse2.332>
- Barazzetti, L., Previtali, M., Cantini, L., & Oteri, A. M. (2023). Digital recording of historical defensive structures in mountainous areas using drones: Considerations and comparisons. *Drones*, 7, 512. <https://doi.org/10.3390/drones7080512>
- Bengtsson, S. B. K., Barklund, P., von Brömssen, C., & Stenlid, J. (2014). Seasonal pattern of lesion development in diseased *Fraxinus excelsior* infected by *Hymenoscyphus pseudoalbidus*. *PLoS One*, 9, e76429. <https://doi.org/10.1371/journal.pone.0076429>
- Berra, E. F., Gaulton, R., & Barr, S. (2016). Use of a digital camera onboard a UAV to monitor spring phenology at individual tree level. In *2016 IEEE International Geoscience and Remote Sensing Symposium (IGARSS)* (pp. 3496–3499). Presented at the 2016 IEEE International Geoscience and Remote Sensing Symposium (IGARSS). <https://doi.org/10.1109/IGARSS.2016.7729904>
- Burt, A., Disney, M., & Calders, K. (2019). Extracting individual trees from lidar point clouds using treeseg. *Methods in Ecology and Evolution*, 10, 438–445. <https://doi.org/10.1111/2041-210X.13121>
- Cessna, J., Alonzo, M. G., Foster, A. C., & Cook, B. D. (2021). Mapping boreal forest spruce beetle health status at the individual crown scale using fused spectral and structural data. *Forests*, 12, 1145. <https://doi.org/10.3390/f12091145>
- Chan, A. H. Y., Barnes, C., Swinfield, T., & Coomes, D. A. (2021). Monitoring ash dieback (*Hymenoscyphus fraxineus*) in British forests using hyperspectral remote sensing. *Remote Sensing in Ecology and Conservation*, 7, 306–320. <https://doi.org/10.1002/rse2.190>
- Cho, M. A., Mathieu, R., Asner, G. P., Naidoo, L., van Aardt, J., Ramoelo, A., Debba, P., Wessels, K., Main, R., Smit, I. P. J., & Erasmus, B. (2012). Mapping tree species composition in South African savannas using an integrated airborne spectral and LiDAR system. *Remote Sensing of Environment*, 125, 214–226. <https://doi.org/10.1016/j.rse.2012.07.010>
- Cleary, M. R., Daniel, G., & Stenlid, J. (2013). Light and scanning electron microscopy studies of the early infection stages of *Hymenoscyphus pseudoalbidus* on *Fraxinus excelsior*. *Plant Pathology*, 62, 1294–1301. <https://doi.org/10.1111/ppa.12048>
- Coker, T. L. R., Rozsypálek, J., Edwards, A., Harwood, T. P., Butfoy, L., & Buggs, R. J. A. (2019). Estimating mortality rates of European ash (*Fraxinus excelsior*) under the ash dieback (*Hymenoscyphus fraxineus*) epidemic. *Plants, People, Planet*, 1, 48–58. <https://doi.org/10.1002/ppp3.11>
- Dalponte, M., Bruzzone, L., & Gianelle, D. (2012). Tree species classification in the Southern Alps based on the fusion of very high geometrical resolution multispectral/hyperspectral images and LiDAR data. *Remote Sensing of Environment*, 123, 258–270. <https://doi.org/10.1016/j.rse.2012.03.013>
- Dandois, J. P., Baker, M., Olano, M., Parker, G., & Ellis, E. (2017). What is the point? Evaluating the structure, color, and semantic traits of computer vision point clouds of vegetation. *Remote Sensing*, 9, 355. <https://doi.org/10.3390/rs9040355>
- Dandois, J. P., & Ellis, E. C. (2013). High spatial resolution three-dimensional mapping of vegetation spectral dynamics using computer vision. *Remote Sensing of Environment*, 136, 259–276. <https://doi.org/10.1016/j.rse.2013.04.005>

- Dandois, J. P., Olano, M., & Ellis, E. (2015). Optimal altitude, overlap, and weather conditions for computer vision UAV estimates of forest structure. *Remote Sensing*, 7, 13895–13920. <https://doi.org/10.3390/rs71013895>
- Danson, F. M., Disney, M. I., Gaulton, R., Schaaf, C., & Strahler, A. (2018). The terrestrial laser scanning revolution in forest ecology. *Interface Focus*, 8, 20180001. <https://doi.org/10.1098/rsfs.2018.0001>
- Elvidge, C. D., & Chen, Z. (1995). Comparison of broad-band and narrow-band red and near-infrared vegetation indices. *Remote Sensing of Environment*, 54, 38–48. [https://doi.org/10.1016/0034-4257\(95\)00132-K](https://doi.org/10.1016/0034-4257(95)00132-K)
- Flynn, W., Grieve, S. W. D., Henshaw, A. J., Owen, H. J. F., & Lines, E. R. (2024). UAV-derived cluster greenness and pathlength of individual trees collected at Marden Park, UK. *Zenodo*. <https://doi.org/10.5281/zenodo.11191314>
- Frey, J., Kovach, K., Stemmler, S., & Koch, B. (2018). UAV photogrammetry of forests as a vulnerable process. A sensitivity analysis for a structure from motion RGB-image pipeline. *Remote Sensing*, 10, 912. <https://doi.org/10.3390/rs10060912>
- Gamon, J. A., Huemmrich, K. F., Wong, C. Y. S., Ensminger, I., Garrity, S., Hollinger, D. Y., Noormets, A., & Peñuelas, J. (2016). A remotely sensed pigment index reveals photosynthetic phenology in evergreen conifers. *Proceedings of the National Academy of Sciences of the United States of America*, 113, 13087–13092. <https://doi.org/10.1073/pnas.1606162113>
- Giri, K., Biswas, T. K., & Sarkar, P. (2021). ECR-DBSCAN: An improved DBSCAN based on computational geometry. *Machine Learning with Applications*, 6, 100148. <https://doi.org/10.1016/j.mlwa.2021.100148>
- Gitelson, A. A., Kaufman, Y. J., & Merzlyak, M. N. (1996). Use of a green channel in remote sensing of global vegetation from EOS-MODIS. *Remote Sensing of Environment*, 58, 289–298. [https://doi.org/10.1016/S0034-4257\(96\)00072-7](https://doi.org/10.1016/S0034-4257(96)00072-7)
- Gombin, J., Vaidyanathan, R., & Agafonkin, V. (2020). *Concaveman: A very fast 2D. Concave Hull Algorithm*.
- Gross, A., Zaffarano, P. L., Duo, A., & Grünig, C. R. (2012). Reproductive mode and life cycle of the ash dieback pathogen *Hymenoscyphus pseudoalbidus*. *Fungal Genetics and Biology*, 49, 977–986. <https://doi.org/10.1016/j.fgb.2012.08.008>
- Habel, K., Grasman, R., Gramacy, R. B., Mozharovskiy, P., & Sterratt, D. C. (2023). *geometry: Mesh generation and surface tessellation*.
- Hill, L., Jones, G., Atkinson, N., Hector, A., Hemery, G., & Brown, N. (2019). The £15 billion cost of ash dieback in Britain. *Current Biology*, 29, R315–R316. <https://doi.org/10.1016/j.cub.2019.03.033>
- Ho, B., Kocer, B. B., & Kovac, M. (2022). Vision based crown loss estimation for individual trees with remote aerial robots. *ISPRS Journal of Photogrammetry and Remote Sensing*, 188, 75–88. <https://doi.org/10.1016/j.isprsjprs.2022.04.002>
- Hopkinson, C., Chasmer, L., Gynan, C., Mahoney, C., & Sitar, M. (2016). Multisensor and multispectral LIDAR characterization and classification of a forest environment. *Canadian Journal of Remote Sensing*, 42, 501–520. <https://doi.org/10.1080/07038992.2016.1196584>
- Jump, A. S., Ruiz-Benito, P., Greenwood, S., Allen, C. D., Kitzberger, T., Fensham, R., Martínez-Vilalta, J., & Lloret, F. (2017). Structural overshoot of tree growth with climate variability and the global spectrum of drought-induced forest dieback. *Global Change Biology*, 23, 3742–3757. <https://doi.org/10.1111/gcb.13636>
- Kantola, T., Vastaranta, M., Yu, X., Lyytikäinen-Saarenmaa, P., Holopainen, M., Talvitie, M., Kaasalainen, S., Solberg, S., & Hyypä, J. (2010). Classification of defoliated trees using tree-level airborne laser scanning data combined with aerial images. *Remote Sensing*, 2, 2665–2679. <https://doi.org/10.3390/rs2122665>
- Kerkech, M., Hafiane, A., & Canals, R. (2018). Deep learning approach with colorimetric spaces and vegetation indices for vine diseases detection in UAV images. *Computers and Electronics in Agriculture*, 155, 237–243. <https://doi.org/10.1016/j.compag.2018.10.006>
- Kirilov, A., Mintun, E., Ravi, N., Mao, H., Rolland, C., Gustafson, L., Xiao, T., Whitehead, S., Berg, A. C., Lo, W.-Y., Dollár, P., & Girshick, R. (2023). *Segment anything*. <https://doi.org/10.48550/arXiv.2304.02633>
- Kräutler, K., & Kirisits, T. (2012). The ash dieback pathogen *Hymenoscyphus pseudoalbidus* is associated with leaf symptoms on ash species (*Fraxinus* spp.). *Journal of Agricultural Extension and Rural Development*, 4, 261–265. <https://doi.org/10.5897/JAERD12.065>
- Krisanski, S., Taskhiri, M. S., Gonzalez Aracil, S., Herries, D., & Turner, P. (2021). Sensor agnostic semantic segmentation of structurally diverse and complex forest point clouds using deep learning. *Remote Sensing*, 13, 1413. <https://doi.org/10.3390/rs13081413>
- Krofcheck, D. J., Litvak, M. E., & Hurteau, M. D. (2019). Allometric relationships for *Quercus gambelii* and *Robinia neomexicana* for biomass estimation following disturbance. *Ecosphere*, 10, e02905. <https://doi.org/10.1002/ecs2.2905>
- Larrinaga, A. R., & Brotons, L. (2019). Greenness indices from a low-cost UAV imagery as tools for monitoring post-fire Forest recovery. *Drones*, 3, 6. <https://doi.org/10.3390/drones3010006>
- Liebold, A. M., Brockerhoff, E. G., Kalisz, S., Nuñez, M. A., Wardle, D. A., & Wingfield, M. J. (2017). Biological invasions in forest ecosystems. *Biological Invasions*, 19, 3437–3458. <https://doi.org/10.1007/s10530-017-1458-5>
- Lines, E. R., Fischer, F. J., Owen, H. J. F., & Jucker, T. (2022). The shape of trees: Reimagining forest ecology in three dimensions with remote sensing. *Journal of Ecology*, 110, 1730–1745. <https://doi.org/10.1111/1365-2745.13944>
- Manfreda, S., McCabe, M. F., Miller, P. E., Lucas, R., Pajuelo Madrigal, V., Mallinis, G., Ben Dor, E., Helman, D., Estes, L., Ciraolo, G., Müllerová, J., Tauro, F., De Lima, M. I., De Lima, J. L. M. P., Maltese, A., Frances, F., Caylor, K., Kohv, M., Perks, M., ... Toth, B. (2018). On the use of unmanned aerial systems for environmental monitoring. *Remote Sensing*, 10, 641. <https://doi.org/10.3390/rs10040641>
- Metheringham, C. L., Plumb, W. J., Stocks, J. J., Kelly, L. J., Gorriç, M. N., Moat, J., Buggs, R. J. A., & Nichols, R. A. (2022). Rapid polygenic adaptation in a wild population of ash trees under a novel fungal epidemic. <https://doi.org/10.1101/2022.08.01.502033>
- Mohan, M., Leite, R. V., & Broadbent, E. N. (2021). Individual tree detection using UAV-lidar and UAV-SfM data: A tutorial for beginners. *Open Geosciences*, 12, 1028–1039.
- Munné-Bosch, S., & Alegre, L. (2004). Die and let live: Leaf senescence contributes to plant survival under drought stress. *Functional Plant Biology*, 31, 203–216. <https://doi.org/10.1071/fp03236>
- Nesbit, P., & Hugenholtz, C. (2019). Enhancing UAV-SfM 3D model accuracy in high-relief landscapes by incorporating oblique images. *Remote Sensing*, 11, 239. <https://doi.org/10.3390/rs11030239>
- Nijland, W., de Jong, R., de Jong, S. M., Wulder, M. A., Bater, C. W., & Coops, N. C. (2014). Monitoring plant condition and phenology using infrared sensitive consumer grade digital cameras. *Agricultural and Forest Meteorology*, 184, 98–106. <https://doi.org/10.1016/j.agrformet.2013.09.007>
- Owen, H. J. F., Flynn, W. R. M., & Lines, E. R. (2021). Competitive drivers of inter-specific deviations of crown morphology from theoretical predictions measured with terrestrial laser scanning. *Journal of Ecology*, 109, 2612–2628. <https://doi.org/10.1111/1365-2745.13670>
- Park, J. Y., Muller-Landau, H. C., Lichstein, J. W., Rifai, S. W., Dandois, J. P., & Bohlman, S. A. (2019). Quantifying leaf phenology of individual trees and species in a tropical forest using unmanned aerial vehicle (UAV) images. *Remote Sensing*, 11, 1534. <https://doi.org/10.3390/rs11131534>
- Pedregosa, F., Varoquaux, G., Gramfort, A., Michel, V., Thirion, B., Grisel, O., Blondel, M., Prettenhofer, P., Weiss, R., Dubourg, V., Vanderplas, J., Passos, A., Cournapeau, D., Brucher, M., Perrot, M., & Duchesnay, E. (2011). Scikit-learn: Machine learning in python. *Journal of Machine Learning Research*, 12, 2825–2830.

- Pliūra, A., Lygis, V., Suchockas, V., & Bartkevičius, E. (2011). Performance of twenty four European *Fraxinus excelsior* populations in three Lithuanian progeny trials with a special emphasis on resistance to Chalara Fraxinea. *Baltic Forestry*, 17, 18.
- R Core Team. (2023). *R: A language and environment for statistical computing*. R Foundation for Statistical Computing.
- Reid, A. M., Chapman, W. K., Prescott, C. E., & Nijland, W. (2016). Using excess greenness and green chromatic coordinate colour indices from aerial images to assess lodgepole pine vigour, mortality and disease occurrence. *Forest Ecology and Management*, 374, 146–153. <https://doi.org/10.1016/j.foreco.2016.05.006>
- Richardson, A. D. (2019). Tracking seasonal rhythms of plants in diverse ecosystems with digital camera imagery. *The New Phytologist*, 222, 1742–1750. <https://doi.org/10.1111/nph.15591>
- Richardson, A. D., Hufkens, K., Milliman, T., Aubrecht, D. M., Chen, M., Gray, J. M., Johnston, M. R., Keenan, T. F., Klosterman, S. T., Kosmala, M., Melaas, E. K., Friedl, M. A., & Frolking, S. (2018). Tracking vegetation phenology across diverse North American biomes using PhenoCam imagery. *Scientific Data*, 5, 180028. <https://doi.org/10.1038/sdata.2018.28>
- Roşca, S., Suomalainen, J., Bartholomeus, H., & Herold, M. (2018). Comparing terrestrial laser scanning and unmanned aerial vehicle structure from motion to assess top of canopy structure in tropical forests. *Interface Focus*, 8, 20170038. <https://doi.org/10.1098/rsfs.2017.0038>
- Rusu, R. B., & Cousins, S. (2011). 3D is here: Point cloud library (PCL). In 2011 IEEE International Conference on Robotics and Automation (Ed.), *Presented at the 2011 IEEE International Conference on Robotics and Automation (ICRA)* (pp. 1–4). IEEE. <https://doi.org/10.1109/ICRA.2011.5980567>
- Sankaran, S., Mishra, A., Ehsani, R., & Davis, C. (2010). A review of advanced techniques for detecting plant diseases. *Computers and Electronics in Agriculture*, 72, 1–13. <https://doi.org/10.1016/j.compag.2010.02.007>
- Sethi, S., Ewers, R. M., & Balakrishnan, R. (2023). Ecology: Correct the digital data divide. *Nature*, 617, 35. <https://doi.org/10.1038/d41586-023-01481-4>
- Seyednasrollah, B., Young, A. M., Hufkens, K., Milliman, T., Friedl, M. A., Frolking, S., & Richardson, A. D. (2019). Tracking vegetation phenology across diverse biomes using version 2.0 of the PhenoCam dataset. *Scientific Data*, 6, 222. <https://doi.org/10.1038/s41597-019-0229-9>
- Shendryk, I., Broich, M., Tulbure, M. G., McGrath, A., Keith, D., & Alexandrov, S. V. (2016). Mapping individual tree health using full-waveform airborne laser scans and imaging spectroscopy: A case study for a floodplain eucalypt forest. *Remote Sensing of Environment*, 187, 202–217. <https://doi.org/10.1016/j.rse.2016.10.014>
- Skovsgaard, J. P., Thomsen, I. M., Skovsgaard, I. M., & Martinussen, T. (2010). Associations among symptoms of dieback in even-aged stands of ash (*Fraxinus excelsior* L.). *Forest Pathology*, 40, 7–18. <https://doi.org/10.1111/j.1439-0329.2009.00599.x>
- Sonntag, O., Hufkens, K., Teshera-Sterne, C., Young, A. M., Friedl, M., Braswell, B. H., Milliman, T., O'Keefe, J., & Richardson, A. D. (2012). Digital repeat photography for phenological research in forest ecosystems. *Agricultural and Forest Meteorology*, 152, 159–177. <https://doi.org/10.1016/j.agrformet.2011.09.009>
- Soudani, K., Delpierre, N., Berveiller, D., Hmimina, G., Pontailier, J.-Y., Seureau, L., Vincent, G., & Dufrêne, É. (2021). A survey of proximal methods for monitoring leaf phenology in temperate deciduous forests. *Biogeosciences*, 18, 3391–3408. <https://doi.org/10.5194/bg-18-3391-2021>
- Stahl, A. T., Andrus, R., Hicke, J. A., Hudak, A. T., Bright, B. C., & Meddens, A. J. H. (2023). Automated attribution of forest disturbance types from remote sensing data: A synthesis. *Remote Sensing of Environment*, 285, 113416. <https://doi.org/10.1016/j.rse.2022.113416>
- Stephenson, N. L., Das, A. J., Ampersee, N. J., Cahill, K. G., Caprio, A. C., Sanders, J. E., & Williams, A. P. (2018). Patterns and correlates of giant sequoia foliage dieback during California's 2012–2016 hotter drought. *Forest Ecology and Management*, 419–420, 268–278. <https://doi.org/10.1016/j.foreco.2017.10.053>
- Stocks, J. J., Buggs, R. J. A., & Lee, S. J. (2017). A first assessment of *Fraxinus excelsior* (common ash) susceptibility to *Hymenoscyphus fraxineus* (ash dieback) throughout the British Isles. *Scientific Reports*, 7, 16546. <https://doi.org/10.1038/s41598-017-16706-6>
- Stone, C., & Mohammed, C. (2017). Application of remote sensing technologies for assessing planted forests damaged by insect pests and fungal pathogens: A review. *Current Forestry Reports*, 3, 75–92. <https://doi.org/10.1007/s40725-017-0056-1>
- Terryn, L., Calders, K., Disney, M., Origo, N., Malhi, Y., Newnham, G., Raunonen, P., Åkerblom, M., & Verbeeck, H. (2020). Tree species classification using structural features derived from terrestrial laser scanning. *ISPRS Journal of Photogrammetry and Remote Sensing*, 168, 170–181. <https://doi.org/10.1016/j.isprsjprs.2020.08.009>
- Timmermann, V., Børja, I., Hietala, A. M., Kirisits, T., & Solheim, H. (2011). Ash dieback: Pathogen spread and diurnal patterns of ascospore dispersal, with special emphasis on Norway*: Ash dieback: Pathogen spread and ascospore dispersal. *EPPO Bulletin*, 41, 14–20. <https://doi.org/10.1111/j.1365-2338.2010.02429.x>
- Tinkham, W. T., & Swayze, N. C. (2021). Influence of Agisoft Metashape parameters on UAS structure from motion individual tree detection from canopy height models. *Forests*, 12, 250. <https://doi.org/10.3390/f12020250>
- Tomaščík, J., Mokroš, M., Surový, P., Grznárová, A., & Merganič, J. (2019). UAV RTK/PPK method—An optimal solution for mapping inaccessible forested areas? *Remote Sensing*, 11, 721. <https://doi.org/10.3390/rs11060721>
- van Iersel, W., Straatsma, M., Addink, E., & Middelkoop, H. (2018). Monitoring height and greenness of non-woody floodplain vegetation with UAV time series. *ISPRS Journal of Photogrammetry and Remote Sensing*, 141, 112–123. <https://doi.org/10.1016/j.isprsjprs.2018.04.011>
- Vicari, M. B., Disney, M., Wilkes, P., Burt, A., Calders, K., & Woodgate, W. (2019). Leaf and wood classification framework for terrestrial LiDAR point clouds. *Methods in Ecology and Evolution*, 10, 680–694. <https://doi.org/10.1111/2041-210X.13144>
- Villari, C., Dowkiw, A., Enderle, R., Ghasemkhani, M., Kirisits, T., Kjær, E. D., Marčiulyrienė, D., McKinney, L. V., Metzler, B., Muñoz, F., Nielsen, L. R., Pliūra, A., Stener, L.-G., Suchockas, V., Rodriguez-Saona, L., Bonello, P., & Cleary, M. (2018). Advanced spectroscopy-based phenotyping offers a potential solution to the ash dieback epidemic. *Scientific Reports*, 8, 17448. <https://doi.org/10.1038/s41598-018-35770-0>
- Vincini, M., & Frazzi, E. (2011). Comparing narrow and broad-band vegetation indices to estimate leaf chlorophyll content in planophile crop canopies. *Precision Agriculture*, 12, 334–344. <https://doi.org/10.1007/s11119-010-9204-3>
- Wang, R., Bowling, D. R., Gamon, J. A., Smith, K. R., Yu, R., Hmimina, G., Ueyama, M., Noormets, A., Kolb, T. E., Richardson, A. D., Bourque, C. P. A., Bracho, R., Blanken, P. D., Black, T. A., & Arain, M. A. (2023). Snow-corrected vegetation indices for improved gross primary productivity assessment in North American evergreen forests. *Agricultural and Forest Meteorology*, 340, 109600. <https://doi.org/10.1016/j.agrformet.2023.109600>
- Wardlaw, T., Bashford, R., Wotherspoon, K., Wylie, R., & Elliot, H. (2008). Effectiveness of routine forest health surveillance in detecting pest and disease damage in eucalypt plantations. *New Zealand Journal of Forestry Science*, 38, 253–269.

- Wielgosz, M., Puliti, S., Wilkes, P., & Astrup, R. (2023). Point2Tree(P2T)—Framework for parameter tuning of semantic and instance segmentation used with mobile laser scanning data in coniferous forest. <https://doi.org/10.48550/arXiv.2305.02651>
- Wilkes, P., Lau, A., Disney, M., Calders, K., Burt, A., Gonzalez de Tanago, J., Bartholomeus, H., Brede, B., & Herold, M. (2017). Data acquisition considerations for terrestrial laser scanning of forest plots. *Remote Sensing of Environment*, 196, 140–153. <https://doi.org/10.1016/j.rse.2017.04.030>
- Yang, X., Tang, J., & Mustard, J. F. (2014). Beyond leaf color: Comparing camera-based phenological metrics with leaf biochemical, biophysical, and spectral properties throughout the growing season of a temperate deciduous forest. *Journal of Geophysical Research: Biogeosciences*, 119, 181–191. <https://doi.org/10.1002/2013JG002460>
- Yu, X., Tang, L., Rao, Y., Huang, T., Zhou, J., & Lu, J. (2022). Point-BERT: Pre-training 3D point cloud transformers with masked point modeling. <https://doi.org/10.48550/arXiv.2111.14819>
- Zhou, Q.-Y., Park, J., & Koltun, V. (2018). Open3D: A modern library for 3D data processing.

SUPPORTING INFORMATION

Additional supporting information can be found online in the Supporting Information section at the end of this article.

Supporting Information S11. Expert visual assessments of crown health.

Figure S11. Histogram showing the number of trees taken from a subset for which we had expert visual assessments of crown health (percent live crown).

Supporting Information S12. Monthly measurements of g_{cc} .

Figure S12. Boxplot plot showing average individual tree g_{cc} measurements taken in September–October 2020 and each month May–August 2021 using a DJI Mavic Mini UAV.

Supporting Information S13. Relationship of g_{cc} values with visual assessments of crown health measured in 2019 and 2020.

Figure S13. The relationship between visual assessment of crown health, defined as percent live crown measured in (a) 2019 and (b) 2020, and green chromatic coordinate (g_{cc}) throughout the growing season.

Table S11. Correlation between visual assessments of tree health carried out in 2019, 2020 and 2021.

Supporting Information S14. Description of forest density and topography.

Figure S14. Digital Terrain Model (DTM) of area and surrounding area of the plot (black line) at Marden Park.

Figure S15. Crown map of trees used in the analysis.

Figure S16. Photograph of the plot understorey captured at Marden Park in May 2021 during the TLS survey, showing vegetation density.

How to cite this article: Flynn, W. R. M., Grieve, S. W. D., Henshaw, A. J., Owen, H. J. F., Buggs, R. J. A., Metheringham, C. L., Plumb, W. J., Stocks, J. J., & Lines, E. R. (2024). UAV-derived greenness and within-crown spatial patterning can detect ash dieback in individual trees. *Ecological Solutions and Evidence*, 5, e12343. <https://doi.org/10.1002/2688-8319.12343>